View metadata, citation and similar papers at core.ac.uk

brought to you by CORE

provided by Institute of Transport Research:Publications

Journal of Applied Remote Sensing

RemoteSensing.SPIEDigitalLibrary.org

On the accuracy gain of electromagnetic wave delay predictions derived by the digital filter initialization technique

Franz-Georg Ulmer

SPIE.

On the accuracy gain of electromagnetic wave delay predictions derived by the digital filter initialization technique

Franz-Georg Ulmer*
Deutsches Zentrum für Luft- und Raumfahrt, Remote Sensing Technology Institute (IMF), Münchener Straße 20, Weßling 82234, Germany

Abstract. Atmosphere causes delay distortions in synthetic aperture radar images. Numerical weather prediction models, which compute the forecast stepwise, are beneficial in correcting this distortion. After initialization, the model needs time to reach a balanced state, such that first prediction steps contain errors. The imbalance causes false predicted precipitation, which then affects the water vapor distribution. Correspondingly, the predicted zenith path delay (ZPD), which depends on this distribution, is affected by the initial imbalances. The digital filtering initialization (DFI) technique reduces these imbalances and the ZPD prediction disturbances, respectively. The objective of this paper is the accuracy gain for ZPD predictions, which is achieved by this technique. For the accuracy gain investigation, predicted ZPD time series of the weather research and forecasting (WRF) model with and without DFI are compared against Global Navigation Satellite System (GNSS)-derived time series from 233 GNSS stations mainly located in Germany. Three conclusions are found. First, the experiment confirms that the DFI technique improves the precipitation forecast. Second, the corresponding accuracy gain, i.e., the bias of ZPD predictions, improves by about 13%. Third, the accuracy gain is only valid for the first 4 h of the prediction. © *The Authors. Published by SPIE under a Creative Commons Attribution 3.0 Unported License. Distribution or reproduction of this work in whole or in part requires full attribution of the original publication, including its DOI.* [DOI: 10.1117/1.JRS.10.016007]

Keywords: weather research and forecasting; numerical weather prediction; spin-up; zenith path delay; GNSS; digital filtering initialization.

Paper 15784 received Nov. 10, 2015; accepted for publication Jan. 8, 2016; published online Feb. 2, 2016.

1 Introduction

Synthetic aperture radar is a popular remote sensing technique for observing Earth's surface. The strength of a signal, which is scattered back, is independent of the actual weather condition, whereas the wave propagation velocity depends on water vapor, pressure, and temperature.[1] Differential interferometric synthetic aperture radar (DInSAR) images are made from subtracted phase information from two synthetic aperture radar acquisitions and, therefore, are affected by weather changes. This spatial effect on the phases is known as the atmospheric phase screen (APS). Also affected is the absolute ranging technique, which considers the total delay of the waves instead of the phase.[2] In recent years, numerical weather predictions (NWPs) have become state-of-the-art in mitigating the atmospheric delays independent of the radar data. Different authors successfully demonstrated the mitigation of the APS using NWP for deformation estimation.[3–7] Similar to DInSAR, the delay correction using NWPs is also beneficial for the absolute ranging technique to estimate displacement maps.[8] Cong et al.[9] demonstrated a straightforward technique by using exclusively the European Centre for Medium-Range Weather Forecasts reanalysis (ECMWF ERA-interim) data, which are also used for the NWP initialization in this work. In comparison to this technique, the model-based prediction technique enables the physical interpolation between time steps. In case of ECMWF ERA-interim data, the time sampling is 6 h and a prediction interpolates temporally as well as spatially in a physically correct way.

*Address all correspondence to: Franz-Georg Ulmer, E-mail: Franz-Georg.Ulmer@dlr.de

Input weather data of a prediction are commonly of coarse resolution, and in this example it is 0.75 deg, which is ≈83 km. Therefore, the initial data must be spatially interpolated for higher resolutions. This interpolation is physically unbalanced, as NWP needs prediction lead time to stabilize.[10] This time is called spin-up time. The weather research and forecasting (WRF) model measures this imbalance by the diagnostic variable dpsdt, which is the domain averaged surface pressure tendency. This variable converges with further integration duration against a stable value, which represents the balanced state (see Fig. 2 at the end of this work). The imbalance disturbs the precipitation forecast at the first prediction hours.[11] This wrongly predicted precipitation disturbs the water vapor distribution, which causes zenith path delay (ZPD) prediction distortions, respectively. The digital filtering initialization (DFI) technique reduces this undesirable behavior[11–13] by integrating backward and/or forward in time, and removes nonphysical high frequencies by using a digital filter.[10] This is particularly helpful for time-critical applications to save computational time. The DFI accuracy gain for ZPD predictions is unknown.

Similar to SAR acquisitions, Global Navigation Satellite System (GNSS)-measured time delays are also affected by the atmosphere and are very accurate and well investigated.[14–16] They provide the ground truth ZPD time series (G_i), because the best agreement between different approaches was achieved by the GNSS and the very long baseline interferometry (with a mean bias of −3.4 mm and a standard deviation of 5.1 mm).[15] For the accuracy gain investigation, the sample mean and the sample standard deviation of the residuals $D_i = F_i - G_i$ are computed, where F_i is the predicted ZPD. The sample means and the sample standard deviations from residues (D_i) of WRF running with and without DFI are then compared.

The objective of this paper is to investigate the accuracy gain of delay predictions derived by the DFI technique, exemplarily at the test site in Germany.

2 Methods

The ground truth in this work is provided by 233 GNSS stations mainly in Germany, their locations are displayed in Fig. 1(b). E-GVAP[17] provides the corresponding ZPD time series (G_i) which were processed by GeoForschungsZentrum. Related to the GNSS time series, the WRF prediction data set consists of 44 predictions with and without DFI. The NWP dates are in-between 14 August, 2011, and 20 June, 2013. All 6-h predictions were initialized at 12 o'clock GMT, have a horizontal resolution of 2.7 km, and cover Germany. This is illustrated by the domain d02 in Fig. 1(a). ECMWF ERA-interim data[18] with 0.75 deg resolution and 6-h time sampling were used as initialization data.

The well-tested parameterization in Chapter 5 of the WRF User's Guide was used.[19] The actual three-dimensional state of the simulated atmosphere was sampled correspondingly to the ground truth G_i. A predicted ZPD time series F_i with a time lag of 15 min was finally derived. This was achieved by the following integration, whereby the temperature as well as the water vapor data were trilinearly interpolated within the grid cells. For pressure, the horizontal data were bilinearly interpolated and, finally, exponentially interpolated in the vertical direction.

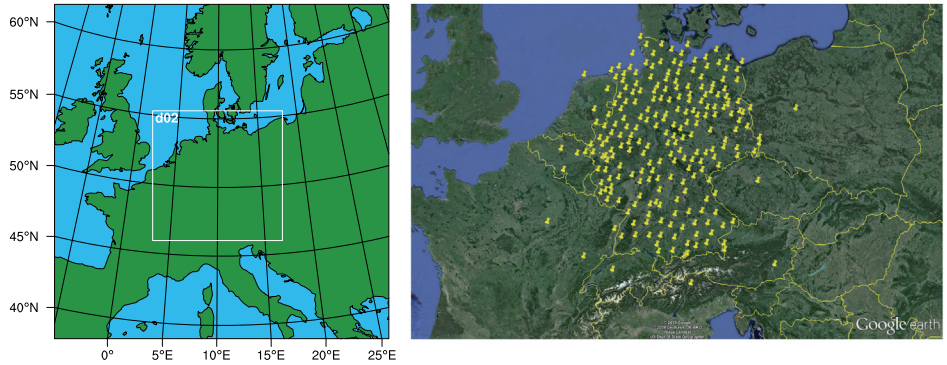

Fig. 1 (a) NWP domain configuration and (b) GNSS station locations.

The predicted ZPD at time i was computed by

$$F_i = 10^{-6} \int_{\vec{z}_0}^{\vec{z}_s} N_a(\vec{z}) \mathrm{d}\vec{z}, \tag{1}$$

where

$$N_a = K_1 \frac{P}{T} + K_2 \frac{e}{T} + K_3 \frac{e}{T^2}, \tag{2}$$

where P is the pressure, e is the partial pressure of water vapor, T is the temperature, and $\vec{z}_s$ is the position of 80 km above the GNSS station location $\vec{z}_0$. The contribution above 80 km is negligible, because at higher altitudes (higher than 6 km) there is hardly any water vapor present, and pressure decreases exponentially. Used coefficients are $K_1 = 77.6890$ K/mbar, $K_2 = -6.3938$ K/mbar, and $K_3 = 3.75463 \times 10^5$ K^2/mbar, and are derived by Rüeger.[20]

The sample means and the sample standard deviations of the residuals $D_i = F_i - G_i$ are computed twice, one with and one without DFI. Respectively, both are compared for the accuracy gain investigation. That the DFI technique is useful for the ZPD prediction follows on from the fact that the DFI technique allows a more realistic initialization of cloud water content, precipitation, and vertical velocity fields.[11–13] The threat score, which is a measure for correctly predicted precipitation, is better if DFI is used.[13] Since precipitation affects the water vapor distribution, it also affects the ZPD prediction and the related residuals. Correspondingly, the DFI technique reduces the residual D_i, which is shown in the following Sec. 3.1.

3 Results

The accuracy gain investigation of the DFI ZPD prediction is divided into two parts. First, the accuracy gain is derived; second, the significance of the statistics is shown.

3.1 *Accuracy Gain Investigation*

WRF predictions without DFI are affected more by physical imbalances in comparison to WRF predictions with DFI.[10,12,13] For the DFI predictions, 1-h backward integration, 1/2-h forward integration, and a Dolph filter (dfi_nfilter = 7) setting were used. The imbalance is measured by the diagnostic variable dpsdt and is averaged over the 44 WRF (version 3.5) predictions at different dates without DFI (DFI_OPT = 0) and with DFI (DFI_OPT = 3). Corresponding pressure tendency functions are shown in Fig. 2. The dashed line corresponds to WRF predictions with DFI and converges quickly against a stable value which represents the balanced state. In comparison, the solid line, which corresponds to the WRF predictions with common initialization, converges more slowly. Finally, both functions come close together at the fourth hour of the

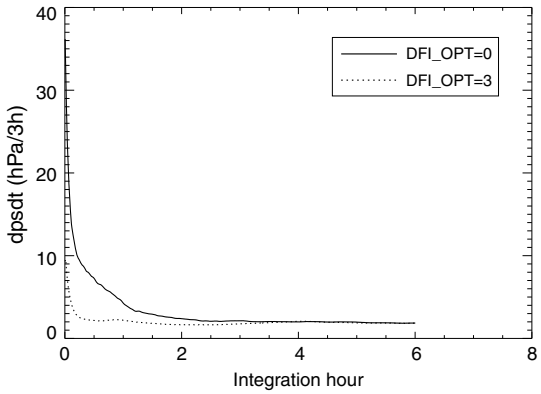

Fig. 2 Domain-averaged surface pressure tendency.

prediction. This point illustrates the average pressure tendency spin-up time of predictions without DFI.

The following accuracy gain investigation is divided into three parts. First, it is shown that the DFI results in a higher water vapor concentration than that of the common initialization. Second, it is shown that this DFI characteristic leads to higher ZPD predictions and, third, that this results in a lower ZPD bias.

3.1.1 *Digital filtering initialization effect on the water vapor concentration*

It is known that WRF predicts too wet forecasts during the first 6 h of integration.[21] It is also known that the threat score of precipitation forecasts is better if the DFI is used instead of the common initialization.[13] In other words, the precipitation forecasts get better if the DFI is used instead of the common initialization. After the initialization, the model builds up clouds, i.e., water vapor condenses. The common initialization results in a higher cloud density and, correspondingly, in a lower water vapor concentration than the DFI. This is illustrated by the histogram in Fig. 3(a). Therefore, the precipitable water vapor (PWV) differences $\hat{R}_i = R_i^{\mathrm{c}} - R_i^{\mathrm{d}}$ of the first prediction hour are computed, where R_i^{c} and R_i^{d} are the PWV data from the common and the DFI technique, respectively. This histogram shows that the PWV R_i^{d} is mostly slightly larger than R_i^{c} ($R_i^{\mathrm{c}} < R_i^{\mathrm{d}}$), because $\hat{R}_i$ is mainly negative and close to zero. In other words, the DFI results mainly in higher water vapor concentrations than those of the common initialization.

3.1.2 *Digital filtering initialization effect on the zenith path delay prediction*

The ZPD F_i can be divided into a hydrostatic H_i and wet component W_i by

$$F_i = H_i + W_i, \tag{3}$$

where H_i is related to the first term and W_i to the next two terms in Eq. (2). Thereby, W_i is related to the PWV R_i by the rule of thumb[16]

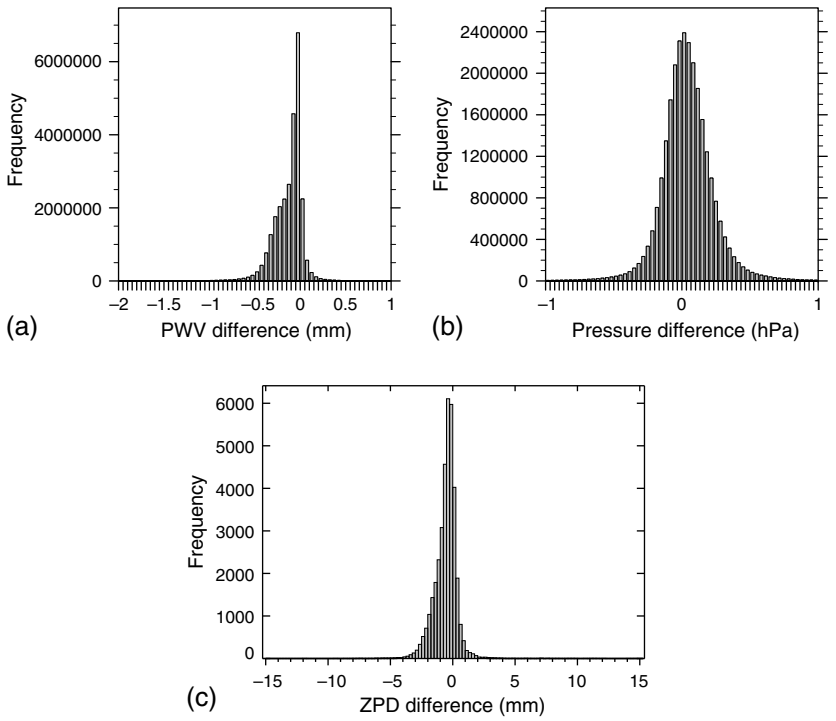

Fig. 3 Difference histogram between the common initialization and the DFI predictions with respect to (a) PWV, (b) pressure, and (c) ZPD.

$$W_i = 6.4R_i. \tag{4}$$

Since $R_i^c < R_i^d$ is mainly valid and because of Eq. (4), $W_i^c < W_i^d$ is mainly valid, where W_i^c and W_i^d are the wet ZPD components of the common and the DFI technique, respectively. Additionally, the hydrostatic component can be approximated by[22,23]

$$H_i = 10^{-6} K_1 \frac{R_d}{g_m} P_s, \tag{5}$$

where $R_d = 287.053\ \mathrm{J\,K^{-1}\,kg^{-1}}$, $g_m = 9.8\ \mathrm{m/s^2}$ and P_s is the surface pressure in hPa. Similar to $\hat{R}_i$, the surface pressure difference $\hat{P}_{si} = P_{si}^c - P_{si}^d$ is computed, where P_{si}^c and P_{si}^d are related to the common initialization and the DFI, respectively. The corresponding histogram is shown in Fig. 3(b) and displays a centered Gaussian distribution with variance of $0.05\ \mathrm{hPa^2}$. Correspondingly, the hydrostatic ZPD change due to the DFI technique is negligible because of the tiny variance and Eq. (5). Consequently, the ZPD delay differences $\hat{F}_i = F_i^c - F_i^d$, where F_i^c and F_i^d are related to the common initialization and the DFI, respectively, result mainly from PWV differences $\hat{R}_i$. Therefore, the $\hat{F}_i$ histogram in Fig. 3(c) has the same shape as the $\hat{R}_i$ histogram in Fig. 3(a), and $F_i^c < F_i^d$ is mainly valid. In other words, the DFI ZPD predictions are inclined toward larger values than the common ZPD predictions.

3.1.3 *Digital filtering initialization effect on the biased zenith path delay prediction*

Up to now, it has been shown that the DFI prevents a stronger condensation of water vapor than that of the common initialization, and results mainly in a higher ZPD prediction. The following shows that the structural higher DFI ZPD prediction reduces the bias of common ZPD prediction. Therefore, the residual D_i sample means are shown in Fig. 4(a) depending on the forecast duration. The DFI sample mean is about 13% better than its counterpart during the first hour. This means that the bias is reduced if the DFI is used instead of the common initialization. This is also illustrated by the residual D_i histogram in Fig. 4(b). The gray-colored histogram corresponds to the common initialization and the over-plotted histogram to the DFI technique. This shows that the gray histogram is more negatively biased than the over-plotted histogram.

I do not compare the sample mean and standard deviation in time, because the accuracy is related to a time of day which influences the prediction accuracy. This is because heating or cooling effects are differently well presented relative to the time of day by WRF.

3.2 *Significance of the Bias Difference*

The following describes the significance of the sample means related to the first integration hour in Fig. 4(a). Commonly, the sample means are close to the real means. This is expressed by a confidence interval around the sample mean that contains the real mean. Unfortunately, this is only true for a given confidence level $(1-\alpha)$, i.e., in $100\alpha\%$ of test cases the confidence interval does not include the real mean. The confidence interval is given by

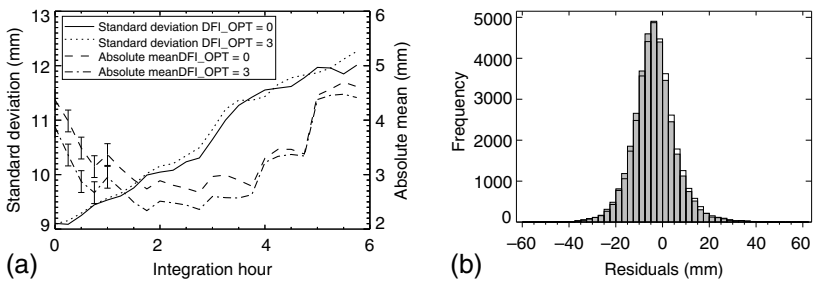

Fig. 4 (a) The mean and standard deviation of the residual D_i with respect to the integration hour and (b) the histogram of them for the first hour.

$$c = \bar{x} \pm z_{\left(1-\frac{\alpha}{2}\right)} \frac{s}{\sqrt{n}}, \tag{6}$$

where $\bar{x}$, s, n, and z_p are the sample mean, the sample standard deviation, the count of observations, and the p-quantile of the standard normal distribution, respectively. In Fig. 4(a), there is $s \leq 9.6$ mm for the first integration hour, and at least $n = 9077$ observations were available. For the superset c_u of the confidence interval c, a confidence level of $1 - \alpha = 0.95$ is assumed. In doing so, $c \subseteq c_u = \bar{x} \pm 0.2$ mm. The confidence intervals are illustrated by bars in Fig. 4(a). The real means are distinct because the confidence intervals do not overlap. Therefore, the difference is significant.

4 Discussion

The ZPD bias reduction indicates a bias reduction with respect to the precipitation forecast. After the fourth hour of the prediction time, the accuracy gain of the DFI technique is vanished, which states that the precipitation forecast quality is then the same for both. Correspondingly, if the time of interest is from 4 to 6 or 10 to 12 either a.m. or p.m. GMT, then the DFI technique is not beneficial for the ZPD and precipitation prediction, because the ERA-interim time sampling is 6 h and starts at midnight GMT. In contrast to the means, the standard deviations in Fig. 4(a) of the DFI and the common initialization are close together. This means that the bias of the precipitation forecast is reduced but the uncertainty with respect to precipitation remains the same.

5 Conclusion

The objective is to investigate the accuracy gain of predicted ZPDs by using the DFI technique at the test site in Germany. Finally, the following three implications are derived. First, the considered experiment confirms that the DFI technique improves the precipitation forecast because the negative bias of the residual D_i is reduced. Second, the accuracy gain of the DFI is a 13% bias reduction of the ZPD prediction. Correspondingly, the biased position estimates, using the absolute ranging and the ZPD prediction technique, improve if the DFI technique is utilized. Third, if the SAR acquisition is from 4 to 6 or 10 to 12 either a.m. or p.m. GMT, then the needed prediction duration is larger than 4 h. Hence, the model is balanced anyway and thus the DFI accuracy gain is invalid. Correspondingly, the common initialization is recommended at that time to save computational time.

Acknowledgments

We thank E-GVAP, the E-GVAP processing centers, and the GNSS data-owners for accessing the E-GVAP NRT GNSS delay data (http://egvap.dmi.dk). Further, we thank Professor Dr. Eineder, Professor Dr. Trautmann, and Christian Minet for discussions and proofreading.

References

1. E. K. Smith and S. Weintraub, "The constants in the equation for atmospheric refractive index at radio frequencies," in *Proc. IRE* **41**(8), 1035–1037 (1953).
2. M. Eineder et al., "Imaging geodesy–toward centimeter-level ranging accuracy with TerraSAR-X," *IEEE Trans. Geosci. Remote Sens.* **49**, 661–671 (2011).
3. R. Holley, G. Wadge, and M. Zhu, "New insights into the nature and effects of the water vapour field on InSAR measurements over Etna," in *Proc. of FRINGE* (2007).
4. J. Jung, D. Kim, and S. E. Park, "Correction of atmospheric phase screen in time series InSAR using WRF model for monitoring volcanic activities," *IEEE Trans. Geosci. Remote Sens.* **52**, 2678–2689 (2014).
5. G. Nico et al., "On the use of the WRF model to mitigate tropospheric phase delay effects in SAR interferograms," *IEEE Trans. Geosci. Remote Sens.* **49**, 4970–4976 (2011).

6. N. Adam, "Algorithmic PSI improvement in mountainous areas by atmosphere mitigation," Technical Report, Issue 3.3, DLR/ESA (2013).
7. F. G. Ulmer and N. Adam, "A synergy method to improve ensemble weather predictions and differential SAR interferograms," *ISPRS J. Photogramm. Remote Sens.* **109**, 98–107 (2015).
8. N. Yague-Martinez et al., "Ground displacement measurement by TerraSAR-X image correlation: the 2011 Tohoku-Oki earthquake," *IEEE Geosci. Remote Sens. Lett.* **9**, 539–543 (2012).
9. X. Cong et al., "Centimeter-level ranging accuracy with TerraSAR-X: an update," *IEEE Geosci. Remote Sens. Lett.* **9**, 948–952 (2012).
10. P. Lynch and X. Y. Huang, "Initialization of the HIRLAM model using a digital filter," *Mon. Weather Rev.* **120**, 1019–1034 (1992).
11. M. Chen and X. Y. Huang, "Digital filter initialization for MM5," *Mon. Weather Rev.* **134**, 1222–1236 (2006).
12. T. Smirnova et al., "Implementation and testing of WRF digital filter initialization (DFI) at NOAA/Earth system research laboratory," in *23rd Conf. on Weather Analysis and Forecasting/19th Conf. on Numerical Weather Prediction* (2009).
13. X. Y. Huang et al., "Development of digital filter initialization for WRF and its implementation at IUM," in *Preprints: 8th Annual WRF Users Workshop* (2007).
14. K. Teke et al., "Multi-technique comparison of troposphere zenith delays and gradients during CONT08," *J. Geod.* **85**(7), 395–413 (2011).
15. K. Teke et al., "Troposphere delays from space geodetic techniques, water vapor radiometers, and numerical weather models over a series of continuous VLBI campaigns," *J. Geod.* **87**(10–12), 981–1001 (2013).
16. M. Bevis et al., "GPS meteorology: remote sensing of atmospheric water vapor using the global positioning system," *J. Geophys. Res.* **97**(D14), 15787–15801 (1992).
17. Met Office, "EIG EUMETNET GNSS water vapour programme (E-GVAP-II)," Technical Report, Issue 1.0, Met Office (2010).
18. D. P. Dee et al., "The ERA-interim reanalysis: configuration and performance of the data assimilation system," *Q. J. R. Meteorol. Soc.* **137**(656), 553–597 (2011).
19. W. Wang et al., "ARW Version 3 modeling system users guide January 2014," Technical Report, Version 3.5, National Center for Atmospheric Research (2013).
20. J. M. Rüeger, "Refractive index formulae for radio waves," in *FIG XXII Int. Congress*, Washington, D.C (2002).
21. I. Jankov et al., "Influence of initial conditions on the WRFARW model QPF response to physical parameterization changes," *Weather Forecasting* **22**, 501–519 (2007).
22. W. Gong et al., "Performance of the high-resolution atmospheric model HRRR-AK for correcting geodetic observations from spaceborne radars," *J. Geophys. Res. Atmos.* **118**(20), 11,611–11,624 (2013).
23. J. L. Davis et al., "Geodesy by radio interfereometry: effects of atmospheric modeling errors on estimates of baseline length," *Radio Sci.* **20**, 1593–1607 (1985).

Franz-Georg Ulmer is a PhD student at the Deutsches Zentrum für Luft- und Raumfahrt. He received his diploma in computer science from the University of Passau in 2010. His current research interests include atmospheric phase screen mitigation for SAR interferometry.